Available online at www.sciencedirect.com

ScienceDirect

Ceramics International 42 (2016) 6154–6167

CERAMICS INTERNATIONAL

www.elsevier.com/locate/ceramint

The field of solid solutions in ternary system of synthetic apatite-type alkaline earth element-yttrium-silicate oxybritholite phases of the composition: $AEE_{\delta}Y_{10-\delta}[SiO_4]_6O_{3-0.5\delta}$, where AEE = Ca, Sr and Ba

Petr Ptáček*, Tomáš Opravil[1], František Šoukal[2], Jakub Tkacz[3], Jiří Másilko[4], Eva Bartoníčková[5]

Brno University of Technology, Faculty of Chemistry, Centre for Materials Research CZ.1.05/2.1.00/01.0012, Purkyňova 464/118, Brno CZ-612 00, Czech Republic

Received 27 November 2015; received in revised form 30 December 2015; accepted 1 January 2016
Available online 8 January 2016

Abstract

This contribution deals with the synthesis, properties and investigation of the field of solid solutions formed between the three end-members of apatite-type alkaline earth element-yttrium-silicate oxybritholites with the hexagonal structure ($P6_3/m$). The stoichiometric composition of these compounds corresponds to the formula $AEE_{\delta}Y_{10-\delta}(SiO_4)_6O_{3-0.5\delta}$, where AEE = Ca, Sr and Ba and parameter $\delta \rightarrow 2$. These compounds and their solid solutions crystallize from non-equilibrium high temperature flux as the main product of sinter-crystallization process. Increasing ionic radius of AEE cations has significant effect to the lattice parameters, properties and miscibility of apatite phases. While there is non-limited miscibility of solid solutions formed between $Ca_2Y_8[SiO_4]_6O_2$ and $Sr_2Y_8[SiO_4]_6O_2$, the highest content of barium in the binary solution with these species is limited to 28% and 38%, respectively. The connecting line of these points marks out the borderline for the field of solid solutions in the ternary system. All attempts for the preparation of pure $Ba_2Y_8[SiO_4]_6O_2$ end-member via the ceramic method were not successful.

Keywords: D. Apatite; Oxybritholite; Yttrium silicates; Solid solution; Sinter-crystallization

1. Introduction

Apatite is the most abundant phosphate mineral, which accounts for more than 95% of total phosphorus (P is the tenth most abundant element on Earth) in the Earth's crust [1]. Sedimentary (80% of total world production) and igneous phosphate rocks are an important mineral commodity used in the chemical industry (manufacturing of phosphorus, phosphoric acid, etc.) and food production (production of phosphate fertilizers) [2]. Furthermore, apatites and their synthetic analogs represent a major class of ionic compounds [3] of interest to many disciplines including medical and biomaterials sciences [4–10], geology [11], cosmology [3], environmental [12] and nuclear sciences [3], preparation of apatite phosphors [13], pigments [14] catalysts in organic synthesis [15] and magneto-optical materials [16].

Apatite is the generic name which was first introduced by German geologist A.G. Werner [17] to describe calcium phosphates of composition given by simplified "*double form*" (**Z** = 2) formula $\mathbf{M}_{10}(\mathbf{TO}_4)_6\mathbf{X}_2$. The "*single form*" is the formula written as $\mathbf{M}_5(\mathbf{TO}_4)_3\mathbf{X}$ [18] where the letters **M** and **X** represent a cation with charge +1, +2 or 3+ (Ca^{2+}, Pb^{2+}, Ba^{2+}, Sr^{2+}, Mn^{2+}, Na^{+}, Ce^{3+}, La^{3+}, Y^{3+}, Bi^{3+} [8]) and monovalent anion (F^{-}, Cl^{-} and OH^{-}), respectively. Cations with charges +4, +5 and +6 (P^{5+}, As^{5+}, V^{5+}, Si^{4+}, S^{6+}, B^{3+} etc.) can occupy the **T** site in the structure of apatite. This

*Corresponding author. Tel.: +420 541 149 389.
E-mail addresses: ptacek@fch.vutbr.cz (P. Ptáček), opravil@fch.vutbr.cz (T. Opravil), soukal@fch.vutbr.cz (F. Šoukal), tkacz@fch.vutbr.cz (J. Tkacz), masilko@fch.vutbr.cz (J. Másilko), bartonickova@fch.vutbr.cz (E. Bartoníčková).
[1]Tel.: +420 541 149 423.
[2]Tel.: +420 541 149 492.
[3]Tel.: +420 541 149 469.
[4]Tel.: +420 541 149 426.
[5]Tel.: +420 541 149 366.

http://dx.doi.org/10.1016/j.ceramint.2016.01.003

composition corresponds to 50 negative charges per unit cell (i.e. 24 O^{2-} +2 (F^-, Cl^- or OH^-)) [3,19–22] and enables partial or complete substitution for cationic (**M**) as well as anionic (**T** and **X**) sites [23,24]. In synthetic compounds with apatite structure, the ***X***-site can be occupied by O^{2-} (oxy-apatite [25,26]) or $(CN_2)^{2-}$ (nitrogen-containing apatite [27]) ions which increase the above-mentioned negative charges per unit cell. On the contrary, the vacancies [28,29] or H_2O molecule [19] on the ***X***-site can decrease the total negative charge depending on the substitutions within the ***M***-site (Cd [30], Co [31], K [32,33] and almost all REE [28, 29,34–38]) and ***T***-site (Be [19], Cr [39,40], Ge [26,41] and Mn^{5+} [19,37]).

The apatite group of minerals is one of five groups categorized in the apatite supergroup of minerals. The other members are hedyphane [42], belovite [43,44], britholite [19,45–47] and ellestadite [19,48–50] groups. Although the kind of original apatite "*sensu lato*" is uncertain the most important minerals of the apatite group are fluorapatite ($Ca_{10}(PO_4)_6F_2$, often abbreviated as FAP [51]), chlorapatite ($Ca_{10}(PO_4)_6Cl_2$, ClAP [52]) and hydroxylapatite ($Ca_{10}(PO_4)_6OH_2$, HAP [53]). These minerals were later renamed as apatite-(CaF), apatite-(CaCl) and apatite-(CaOH) [19,54], respectively. Currently the mineral names are changed back to fluorapatite, chlorapatite and hydroxylapatite [19]. The nomenclature and the classification (approved by the IMA Commission on New Minerals) of the apatite supergroup minerals is described by Pasero et al. [19].

The crystal structure of apatite ("*sensu stricto*" fluorapatite) was first independently solved in 1930 by Mehmel [55] and Náray-Szabó [56]. The archetype of crystalline structure is hexagonal (space group **$P6_3/m$**) and contains the species-defining cation in two crystallographic sites: **M**(1) and **M**(2) with the Wyckoff position of ***4f*** and ***6h***, respectively. **M**(1) site is nine-fold coordinated (6+3) and forms a polyhedron which is often referred to as the metaprism [19,40,57–59] and described as distorted pentagonal bipyramid [19,21]. **M**(2) site shows seven-fold (6+1) coordination. The unit-cell parameters are a=9.3–9.6 Å and c=6.7–6.9 Å [19]. With respect to the structure of apatite-type compounds (Fig. 1(a)), the generic formula can be written as [19,59,60]: $^{IX}\mathbf{M}(1)_2^{VII}\mathbf{M}(2)_3(^{IV}\mathbf{TO}_4)_3\mathbf{X}$ (**Z**=2). The left superscript introduces an ideal coordination number [19]. The monoclinic ($P2_1/b$) variant (it is not considered for distinct species [3,18] from the hexagonal variant) of hydroxylapatite (clinohydroxylapatite [61]) and chlorapatite was formerly named as apatite-(CaOH)-M and apatite-(CaCl)-M [54], respectively. Latterly they were renamed as hydroxylapatite-M and chlorapatite-M [19,54,62].

Britholite (first described by Winther [45]) is one of more common and economically important rare earth element (REE) bearing minerals. The structures of monoclinic ($P2_1$ [63], Fig. 1(b)) and hexagonal ($P6_3$) dimorphs of britholite are similar to the atomic arrangement of apatite (a). The first structural investigation concluded a hexagonal apatite substructure ($P6_3$) [64]. Noe et al. [63] solved the crystal structure of monoclinic dimorph with similar atomic arrangement to apatite and explained the biaxial optical characteristics of britholite by the reduction of symmetry (removing the 3/m element from hexagonal $P6_3/m$ apatite symmetry yielding to monoclinic $P2_1$ symmetry). Monoclinic and hexagonal dimorphs of natural phase exist as a result of differing arrangements of long and short equivalents of the apatite Ca(1)–O(3) bonds [63].

The preparation of numerous compounds with the apatite-type structure including synthetic analogs of apatites [65], britholites [21,22,66,67], belovites [68], etc., and their solid solutions [69] was described in the literature. Usually applied methods involve the high-temperature solid-state synthesis [4,21,22,66], the sol–gel process [4,16], the precipitation method [4,70], the hydrothermal [69–71] or mechanochemical hydrothermal synthesis [9], the citrate gel pyrolysis method [10], the combustion method [65], the microwave processing [4] and the emulsion methods [4,72], etc. The preparation techniques based on aqueous precipitation at moderate temperatures often lead to non-stoichiometric apatites [3].

In the previous work [34], the synthesis, properties and the role of non-equilibrium flux formed during the sinter-crystallization process of $SrY_4(SiO_4)_3O$ (or by "double formula" the $Sr_2Y_8(SiO_4)_6O_2$) oxyapatite phase was described. This contribution deals with the preparation, properties and examination of the field of solid solutions miscibility between three end-members of alkaline earth element-yttrium-silicate phases ($AEE_\delta Y_{10-\delta}(SiO_4)_6O_{3-0.5\delta}$, where AEE=Ca, Sr and Ba and the value of $\delta \rightarrow 2$). The course of synthesis was

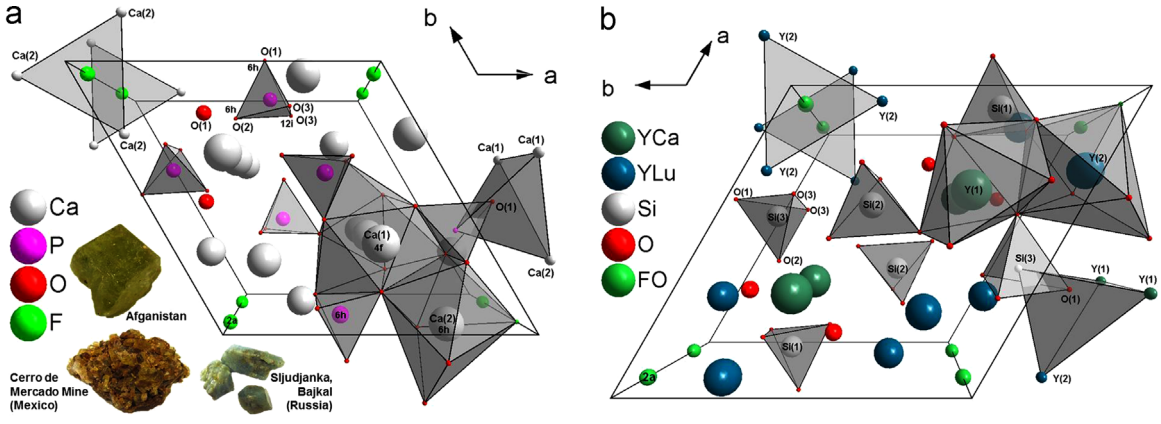

Fig. 1. The structure of fluorapatite (a, perspective view along the c-axis, i.e. from [001]) according to Hughes et al. [58] displayed with the examples of Ca(1), Ca(2), F and O(1) polyhedra. The structure of monoclinic britholite-(Y) (b, perspective) solved by Noe et al. [63].

investigated by the methods of thermal analysis, X-ray diffraction analysis, infrared spectroscopy and electron microscopy. These results were used for the definition of range of miscibility region of ternary solid solutions and for the investigation of effect of AEE^{2+} cation on the system stoichiometry, i.e. the variation of parameter δ in the formula of apatite unit and the lattice parameters.

2. Experimental

2.1. Synthesis of samples

Raw meals for the syntheses of apatite phases were prepared via ceramic route by mixing calcium ($CaCO_3$) strontium ($SrCO_3$) and barium carbonate ($BaCO_3$), yttrium oxide (Y_2O_3) and silica (SiO_2) in the molar ratio (1:2:3) which corresponds to the ideal stoichiometry of reaction [34,73]:

$$AEECO_3 + 2Y_2O_3 + 3SiO_2 \rightarrow AEEY_4(SiO_4)_3O + CO_2(g) \quad (1)$$

where AEE denotes alkaline earth element (Ca_x, Sr_y and Ba_z, where $x+y+z=1$). All chemicals were of analytical purity grade and used without further purification or treatment. The composition and numeric notation of prepared samples (**S1–S18**, e.g. **S1** is pure end-member of $Ca_2Y_8(SiO_4)_6O_2$ phase) are introduced in Fig. 2(a).

Mixing and short milling (2 min) in laboratory ball mill was applied for initial homogenization of raw meal. The flowchart in Fig. 2(b) explains the preparation of raw meal and introduces the conditions of pressing and thermal treatment.

2.2. Investigation of the course of synthesis and properties of prepared samples

The course of synthesis of AEE apatite-type yttrium silicate phases during thermal treatment was investigated by TG–DTA and EGA (SDT Q600, Thermal Instruments connected with the measuring cell (FTIR-TGA interface) of infrared spectrometer iS10, Thermo Scientific via steel capillary). 30 mg of sample was inserted into alumina cup heated in air (100 $cm^3\ min^{-1}$ free of CO_2 and water vapor) with the rate of 10 °C min^{-1}. The process of sinter-crystallization of apatite phase was investigated by heating microscopy (EM 201, Leitz) using cylindrical specimen with the diameter and the height of 3 mm, which was pressed out from raw meal under the pressure of 1 MPa. The changes in the phase composition during thermal treatment were evaluated by high temperature X-ray analysis (XRD, X'Pert Empyrean, PANanalytical with Cu(K_α) radiation at 40 kV and the current of 30 mA applying high temperature chamber HTK 16, Anton Paar). Scanning electron microscopy with EDX (SEM, Zeis EVO LS10 with W-cathode) was used for the analysis of sample after the thermal treatment.

The average of linear expansion coefficient (α_L(25–1500 °C)) was determined from the results of heating microscopy of sintered specimen. The thermal conductivity (λ) was measured by C-ThermTci analyzer at the temperature of 25 °C using Silicone 120 (Wakefield) as thermal joint compound. HSC v.7.1 software was used for the estimation of thermodynamic (TD) data including standard formation enthalpy (ΔH_f°) and Gibbs free energy (ΔG_f°), entropy (S°) and molar heat capacity ($c_{p,m}^\circ$) at the temperature of 298 K and the pressure of 1 bar.

3. Results and discussion

3.1. The end-member phases

The end-member phases in the investigated ternary diagram of alkaline earth element-yttrium-silicate oxybritholite system (Fig. 2(a), samples **S1**, **S2** and **S3**) have stoichiometric composition given by the formula $AEE_\delta Y_{10-\delta}(SiO_4)_6O_{3-0.5\delta}$, where AEE=Ca, Sr and Ba and $\delta \rightarrow 2$. That leads to three compounds with the composition:

1) $Ca_2Y_8(SiO_4)_6O_2$ (dicalcium octayttrium(III) (hexakis) silicate dioxide, **S1**);

2) $Sr_2Y_8(SiO_4)_6O_2$ [34,73] (distrontium octayttrium(III) (hexakis)silicate dioxide, **S2**);

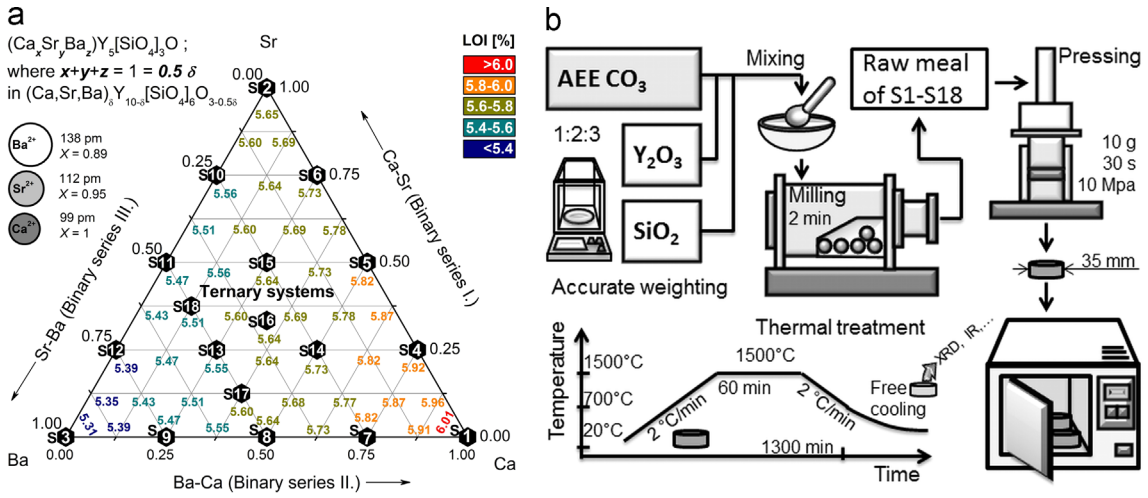

Fig. 2. The composition of prepared samples introduced together with theoretical (calculated from Eq. (1)) value of Loss on Ignition (LOI) during thermal treatment (a). Flowchart used for the preparation of specimens (b).

3) $Ba_2Y_8(SiO_4)_6O_2$ (dibarium octayttrium(III) (hexakis)silicate dioxide, **S3**).

The values of parameter δ resulting from elemental analysis of phases **S1** and **S2** (please refer to Table 2) are 2.02 ± 0.07 and 1.90 ± 0.04, respectively. That means that the composition of these samples is almost stoichiometric. The compound **S3** cannot be prepared for the reasons discussed below, there is an option to prepare binary and ternary solutions of this phase, which is discussed in Sections 3.2 and 3.3.

Fig. 3(a) shows the results of TG–DTA and EGA of raw meal. The endothermic peak at the temperature of 573 °C results from reversible athermal (displacive) transformation between low quartz (trigonal α-SiO_2) and high quartz (hexagonal β-SiO_2) polymorphs of SiO_2 [74]. This process is followed by endothermic peak of thermal decomposition of $AEECO_3$:

$$AEECO_3 \overset{T}{\Longrightarrow} AEEO + CO_2(g), \quad AEE = Ca,\ Sr \text{ and } Ba \qquad (2)$$

While the peak temperature increases with increasing thermal stability of carbonate [75], the measured weight loss decreases with increasing molecular weight of carbonate (please consult with Fig. 3(a)).

The thermal decomposition of calcium, strontium and barium carbonates shows endothermic peaks at the temperatures of 747 (**S1**), 963 (**S2**) and 1000 °C (**S3**), respectively. The transformation to high-temperature polymorphs takes place during the thermal decomposition of $SrCO_3$ and $BaCO_3$. Orthorhombic polymorph of α-$SrCO_3$ (*Pmcn*) transforms to hexagonal form of β-$SrCO_3$. The process shows sharp endothermic peak at the temperature of 931 °C [75,76]. Polymorphic transformation of orthorhombic α-$BaCO_3$ (*Pmcn*) into hexagonal β-$BaCO_3$ (R3m) [77,78] and next to cubic γ-$BaCO_3$ phase [79] takes place at the temperature of 828 and 960 °C, respectively.

Thermal decomposition of carbonates increases the intensity of CO_2 bands on EGA plot (Fig. 3(a)). The strong central bands of antisymmetric stretching mode (ν_3) and degenerated bending mode (ν_2) are located within the wavenumber intervals from 2400 to 2220 cm^{-1} and from 760 to 575 cm^{-1}, respectively. The small peaks within the wavenumber intervals from 3770 to 3655 cm^{-1} and from 3656 to 3535 cm^{-1} are the $\nu_1+\nu_3$ and $2\nu_2+\nu_3$ combination bands, respectively [76].

The formation of intermediate phases appearing within the temperature interval which is limited by the temperature of thermal decomposition of carbonate and sinter-crystallization of apatite phase (**S1** and **S2**) or yttrium oxyorthosilicate (**S3**) was investigated by HT-XRD. The results for phases **S1** and **S3** are shown in Fig. 4 (the behavior of sample **S2** during thermal treatment is described in previous work [34]).

Thermal decomposition of carbonates (Eq. (2)) leads to the formation of oxide species, which means that the diffraction

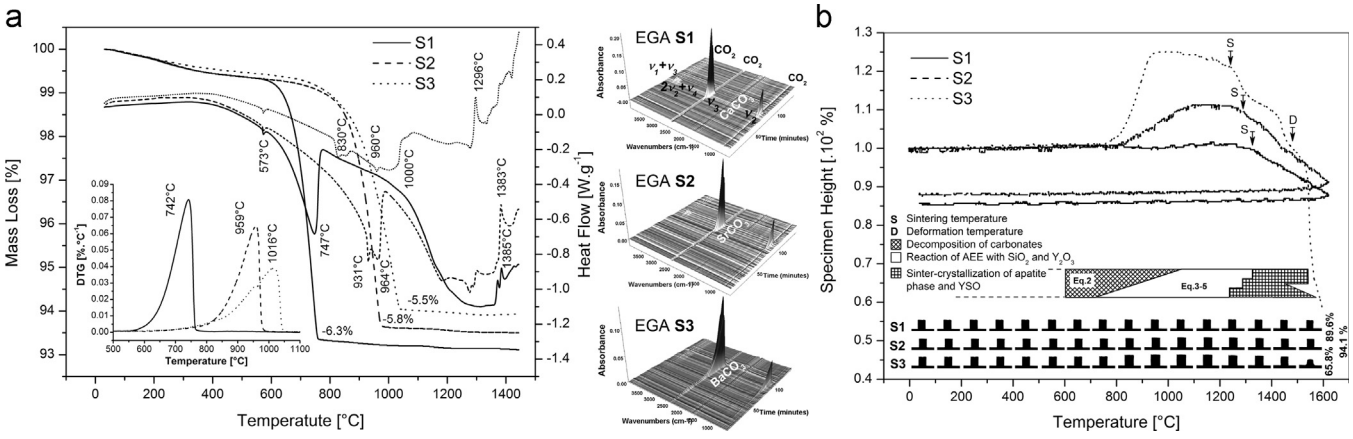

Fig. 3. Simultaneous TG–DTA and EGA (a) and heating microscopy (b) of raw meal for end-members phases in the investigated system of $AEE_\delta Y_{10-\delta}(SiO_4)_6O_{3-0.5\delta}$ apatites: solid line (**S1**), dashed line (**S2**) and dotted line (**S3**).

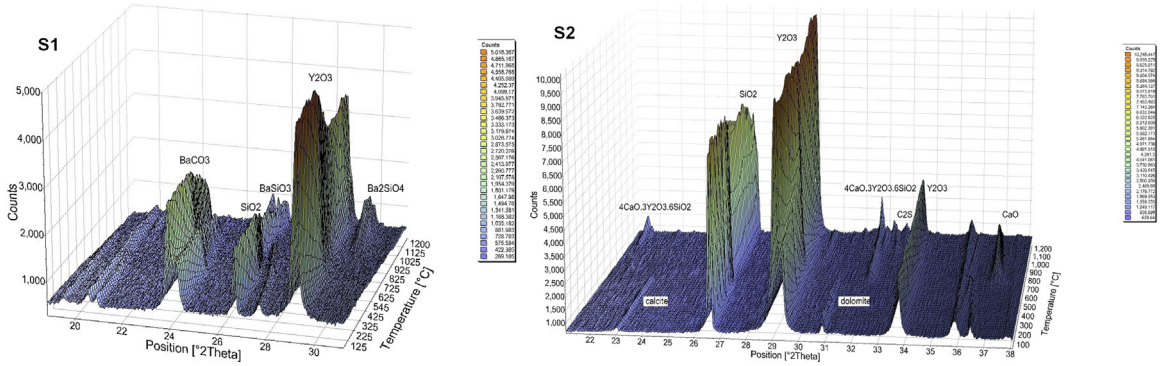

Fig. 4. HT-XRD analysis of raw meals for samples S1 and S3.

lines of CaO ($T \geq 600$ °C) and BaO ($T \geq 675$ °C) appear. The features of $CaCO_3$ and $BaCO_3$ gradually disappear by the temperature of 750 and 1050 °C, respectively. CaO (**S1**, $T \geq 900$ °C) and BaO (**S3**, $T \geq 800$ °C) oxides react with SiO_2 to form alkaline earth orthosilicates (AEE_2SiO_4):

$$2AEEO + SiO_2 \overset{T}{\Longrightarrow} AEE_2SiO_4 \quad (3)$$

While the reaction of Ca_2SiO_4 with Y_2O_3 in sample **S1** leads to the formation of hexagonal ternary calcium yttrium silicate oxide phase of $4CaO \cdot 3Y_2O_3 \cdot 6SiO_2$ ($P6_3/m$), orthosilicate Ba_2SiO_4 in sample **S3** reacts with SiO_2 to form orthorhombic metasilicate $BaSiO_3$:

$$2Ca_2SiO_4 + 3Y_2O_3 + 2SiO_2 \overset{T \geq 1000\ ^\circ C}{\Longrightarrow} Ca_4Y_6O(SiO_4)_6 \quad (4)$$

$$Ba_2SiO_4 + SiO_2 \overset{T \geq 1050\ ^\circ C}{\Longrightarrow} 2BaSiO_3 \quad (5)$$

The results of heating microscopy (Fig. 3(b)) show that the formation of these compounds significantly increases the specimen height for samples **S2** and **S3**, while the changes measured for **S1** are negligible. The sintering temperature decreases in the order **S1**, **S2** and **S3**. Large amount of formed melt phase leads to the deformation of **S3** specimen at the temperature of 1480 °C and to the highest measured value of firing shrinkage.

The formation of high-temperature flux and sinter-crystallization of apatite phase (samples **S1** and **S2** [34]) or yttrium oxyorthosilicate ($Y_2O_3 \cdot SiO_2$, YSO [80,81]) in sample **S3** starts by endothermic effect (melting), which transforms to exothermic peak (crystallization) at the temperature of 1385, 1383 and 1296 °C (Fig. 3(a)), respectively. The process of sinter-crystallization is connected with shrinkage, which increases in the order from **S1** to **S3**.

The SEM analysis of samples **S1** and **S2** (Fig. 5) revealed hexagonal prisms terminated by basal pinacoids (pyramid forms are not present) of $Ca_2Y_8[SiO_4]_6O_2$ and $Sr_2Y_8[SiO_4]_6O_2$ crystals, respectively. These crystals are surrounded by solidified glass-like phase and often fill the space of ceramic body as clusters, where the hexagonal prisms are arranged to the hexagonal prismatic honeycomb.

The decreasing value of Y_2O_3 to SiO_2 (Y/S) ratio and/or the presence of additives [34] improve the morphology of apatite crystals (please compare Fig. 5 and Fig. 6 where Y/S = 0.67 and 0.50, respectively). Some $Ca_2Y_8[SiO_4]_6O_2$ prisms in Fig. 6, terminated by pyramid Sample **S3** (Fig. 5) show the formation of crystals of yttrium oxyorthosilicate (1) surrounded by glassy phase with high content of barium (2).

Standard formation energies, entropies and molar heat capacities estimated for pure end-members are listed in Table 1. The value of ΔG_f° shows decreasing stability in the order **S1** ($r_{Ca}^{2+} = 99$ pm, $X = 1$) > **S2** ($r_{Sr}^{2+} = 112$ pm, $X = 0.95$) > **S3** ($r_{Ba}^{2+} = 138$ pm, $X = 0.89$), so the TD stability decreases with increasing AEE^{2+} ionic radius ($R^2 = 0.993$) and increasing ionic character of AEE–O bond ($R^2 = 0.952$) estimated from Pauling's approximation ($100 \cdot [1 - e^{-1/4(\Delta X)}]$, where ΔX is the difference in Pauling's electronegativity of AEE and O^{2-} (3.44)). This behavior is in agreement with the effect of ΔX between M^{2+} and X^- as well as with general AEE stability tendency of apatite minerals (Ca > Sr > Ba) described by Drouet [3].

3.2. Binary systems

The sides of ternary diagram (Fig. 2) constitute of three binary systems of $AEE_\delta Y_{10-\delta}(SiO_4)_6O_{3-0.5\delta}$ oxybritholite phases, where AEE = Ca–Sr (samples **S4–S6**), Ca–Ba (**S7–S9**) and Sr–Ba (**S10–S12**). The results of TG–DTA and EGA analysis (a) and heating microscopy (b) for these samples are shown in Fig. 7. Whereas the temperature intervals of thermal

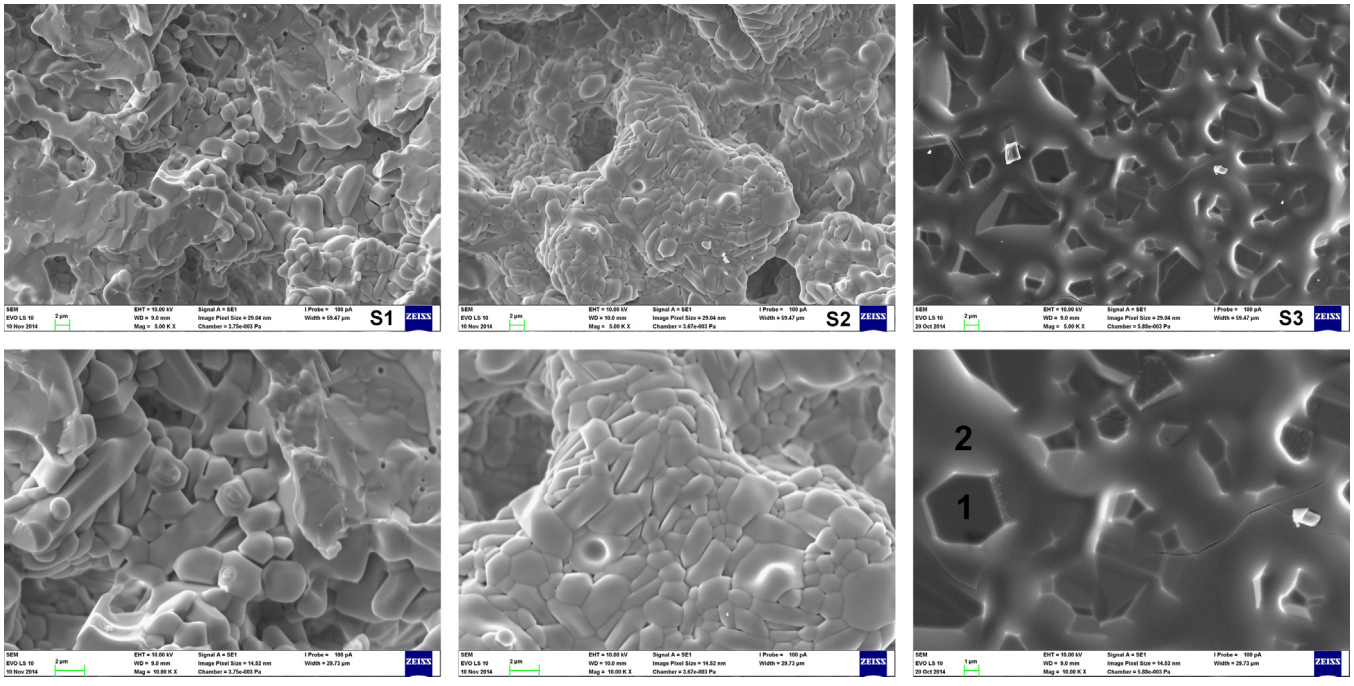

Fig. 5. Scanning electron microscopy of samples S1, S2 and S3 treated to the temperature of 1600 °C.

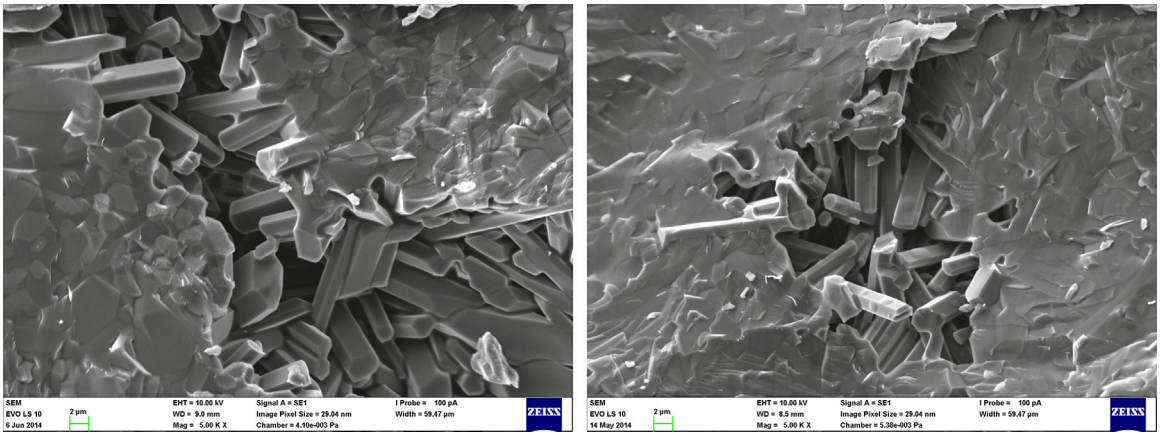

Fig. 6. The crystals of $Ca_{\delta}Y_{10-\delta}[SiO_4]_6O_{3-0.5\delta}$ and $Sr_{\delta}Y_{10-\delta}[SiO_4]_6O_{3-0.5\delta}$ [34] prepared with Y/S ratio of 0.50.

Table 1
Thermodynamic data estimated (HSC) for pure end-members (**S1**, **S2** and **S3**) at 298 K and 1 bar.

Sample		M [g mol^{-1}]	ΔH_f° [J mol^{-1}]	S [J mol^{-1} K^{-1}]	ΔG_f [J mol^{-1}]	$c_{p,m}$ [J mol^{-1} K^{-1}]
S1	$Ca_2Y_8[SiO_4]_6O_2$	1375.90	−14,669.9	691.1	−14,875.8	730.9/728.0[a]
S2	$Sr_2Y_8[SiO_4]_6O_2$	1470.98	−14,645.9	720.6	−14,860.6	736.2/729.7[a]
S3	$Ba_2Y_8[SiO_4]_6O_2$	1570.40	−14,597.3	736.5	−816.8	738.3/731.5[a]

[a]Value estimated by the Latimer method [82,83].

decomposition of $SrCO_3$ and $BaCO_3$ are overlap each other, the temperature of thermal decomposition of $CaCO_3$ is significantly lower (please consult with the detail of Fig. 3). For that reason, two endothermic effects can be recognized on DTA in samples from the Ca–Sr and Ca–Ba series. Also the results of TG and EGA show two separate effects in the order of increasing content and thermal stability of carbonate.

The temperature of sinter-crystallization is reduced with increasing content of $Ca_2Y_8[SiO_4]_6O_2$ in Ca–Sr series. Since total composition of samples **S8**, **S9**, **S11** and **S12** is located out of the field of solid solutions (Fig. 12(a)), the highest intensity of sinter-crystallization effect in the Ca–Ba and Sr–Ba series can be observed in samples **S7** and **S10**. This behavior, as results from the comparison of results of SEM analysis (Fig. 8) with the end-member apatite species (Fig. 5), indicates that barium partially acts as sintering additive [34] which improves the morphology of formed $AEE_{\delta}Y_{10-\delta}(SiO_4)_6O_{3-0.5\delta}$ crystals.

The values of parameter $\boldsymbol{\delta}$ determined from the compositions of pure and binary phases (Fig. 8) are listed in Table 2. The results ($\boldsymbol{\delta} \approx 2$) indicate that the compositions of prepared specimens are close to stoichiometric ones. Fig. 12(a) shows that there is unlimited $Ca^{2+} \leftrightarrow Sr^{2+}$ substitution in the binary system of $(Ca–Sr)_{\delta}Y_{10-\delta}[SiO_4]_3O_{3-0.5\delta}$. On the contrary, the $Ba_{\delta}Y_{10-\delta}[SiO_4]_3O_{3-0.5\delta}$ analog (**S3**) of **S1** and **S2** apatite-type phase cannot be prepared via applied ceramic route, as the extend of $Ca^{2+} \leftrightarrow Ba^{2+}$ and $Sr^{2+} \leftrightarrow Ba^{2+}$ substitutions is limited to 28 ± 4 and 38 ± 4 mol%, respectively.

Higher content of Ba in binary series III can be explained by the selectivity of REE for Ca-bearing minerals and by progressive change of REE preference for M(2) site (Fig. 1(a)) through the 4*f* transition series. It decreases from La to Er and the behavior of Y (please see Fig. 1(b)) is here similar to that of Ho [84]. Another strong evidence that the changes in site preference (whether 4*f* or 6*h*) of REE may influence the stability of Ca-bearing phases (minerals) are the syntheses of $Ba_{2x}La_{8-x}(SiO_4)_6O_{2-\delta}$ and $Ca_2Ce_8(SiO_4)_6O_2$ oxyapatites described by Takeda et al. [85] and Skakle et al. [86], respectively.

3.3. Ternary systems

The results of TG–DTA and EGA analyses of ternary systems **S13–S18** are shown in Fig. 9(a). The low ($\boldsymbol{\alpha}$) to high ($\boldsymbol{\beta}$) transformation of quartz shows small endothermic peak at the temperature of 573 °C. With increasing temperate, the features related to the thermal decomposition of alkaline earth carbonates appear according to increasing thermal stability. Depending on the sample composition, two or three peaks of CO_2 appear on EGA. Similarly to the binary systems, the intensity of sinter-crystallization effect is reduced for the samples out of the miscibility region (samples **S13**, **S17** and **S18**).

Heating microscopy (Fig. 9(b)) shows that the expansion caused by series of decomposition and synthesis processes (Eqs. (2)–(5)) increases with the content of strontium in the sample. The sintering and deformation temperature increases with increasing content of barium in the sample.

Results from scanning electron microscopy and from EDX analysis of samples located inside and out of determined field of solid solutions (Fig. 12(a)) are shown in Figs. 10 and 11, respectively. The crystals formed in sample **S14** are considerably smaller than those observed in other specimens. The

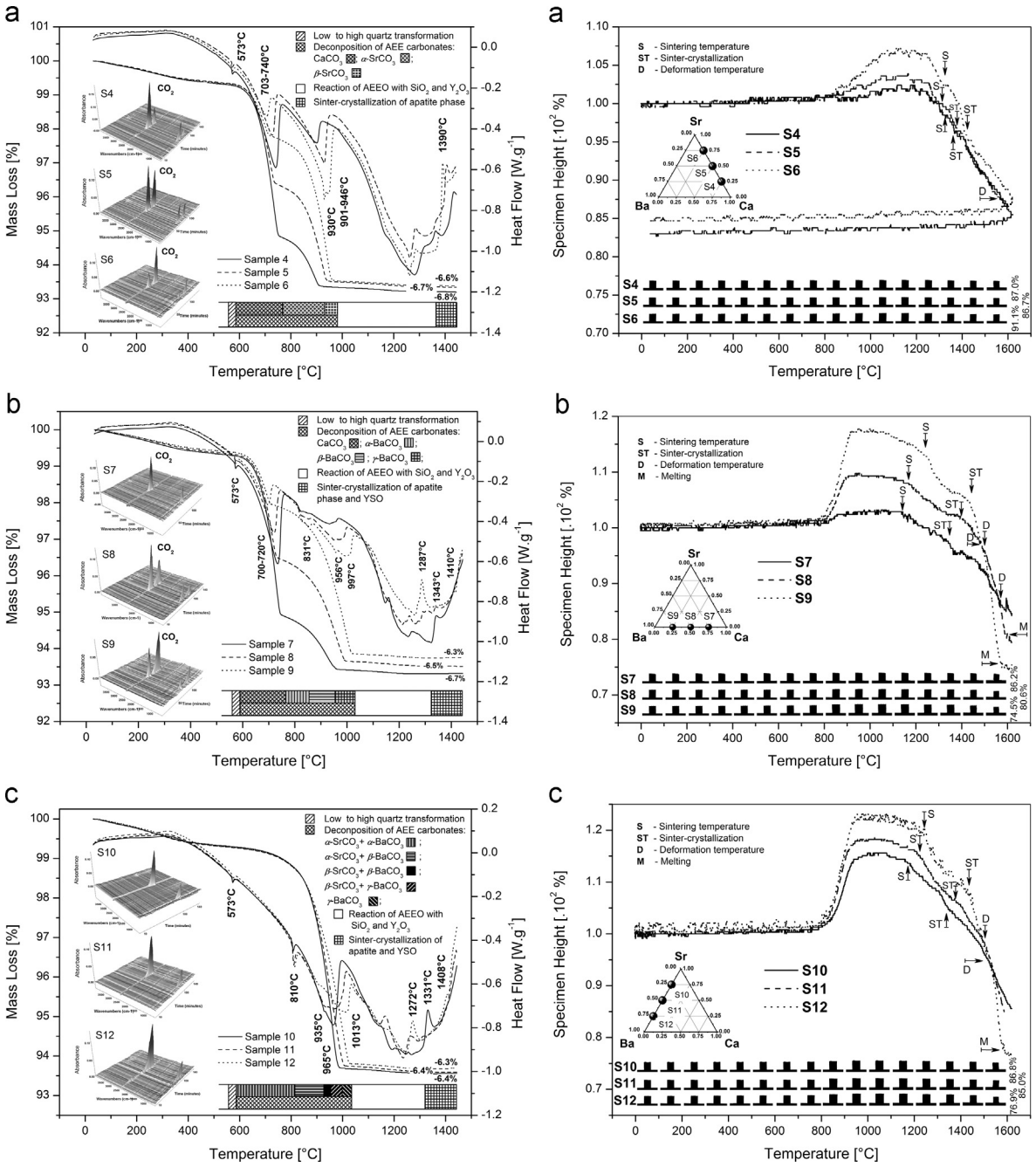

Fig. 7. Thermal analysis of binary systems S1, S2 and S3 (Fig. 2): $(Ca–Sr)_{\delta}Y_{10-\delta}[SiO_4]_6O_{3-0.5\delta}$ (a), $(Ca–Ba)_{\delta}Y_{10-\delta}[SiO_4]_6O_{3-0.5\delta}$ (b) and $(Sr–Ba)_{\delta}Y_{10-\delta}[SiO_4]_6O_{3-0.5\delta}$ (c).

formation of larger amount of smaller crystals indicates enhanced nucleation ability in the melt of this composition. The values of parameter $\boldsymbol{\delta}$ for the crystals of $AEE_{\delta}Y_{10-\delta}(SiO_4)_6O_{3-0.5\delta}$ formed in the ternary region listed in Table 3 do not show any significant differences from the system stoichiometry.

The highest determined content of barium in the apatite-type AEE–yttrium orthosilicate oxybritholites crystals enables to evaluate the borders of field of solid solutions for samples located out of the field of solid solutions (Fig. 11). These data were used for the construction of ternary diagram in Fig. 12(a). Since the composition of $AEE_2Y_8[SiO_4]_6O_2$ phase can be derived from $Y_{10}[SiO_4]_6O_2$ [87] or more precisely from $Y_{9.333}[SiO_4]_6O_2$ (please check both formulas for the average oxidation state of Si atom) via the substitution of 1.333 yttrium atoms by two AEE ($AEE^{2+} \leftrightarrow 2/3\ Y^{3+}$) and the solid solution of $AEE_{\delta}Y_{10-\delta}[SiO_4]_6O_{3-0.5\delta}$ is in the equilibrium with $Y_2O_3 \cdot SiO_2$, the relationship of investigated field of solid solutions with related phase equilibrium system is shown in detail (b). The results in detail (c) reveal that samples with $\boldsymbol{r}^{2+}_{AEE}/\boldsymbol{r}^{4+}_{Si}$ ionic radius ratio ≥ 2.96 are located out of the field of solid solutions. Therefore $\boldsymbol{r}^{2+}_{AEE}/\boldsymbol{r}^{4+}_{Si}$ ratio is an important

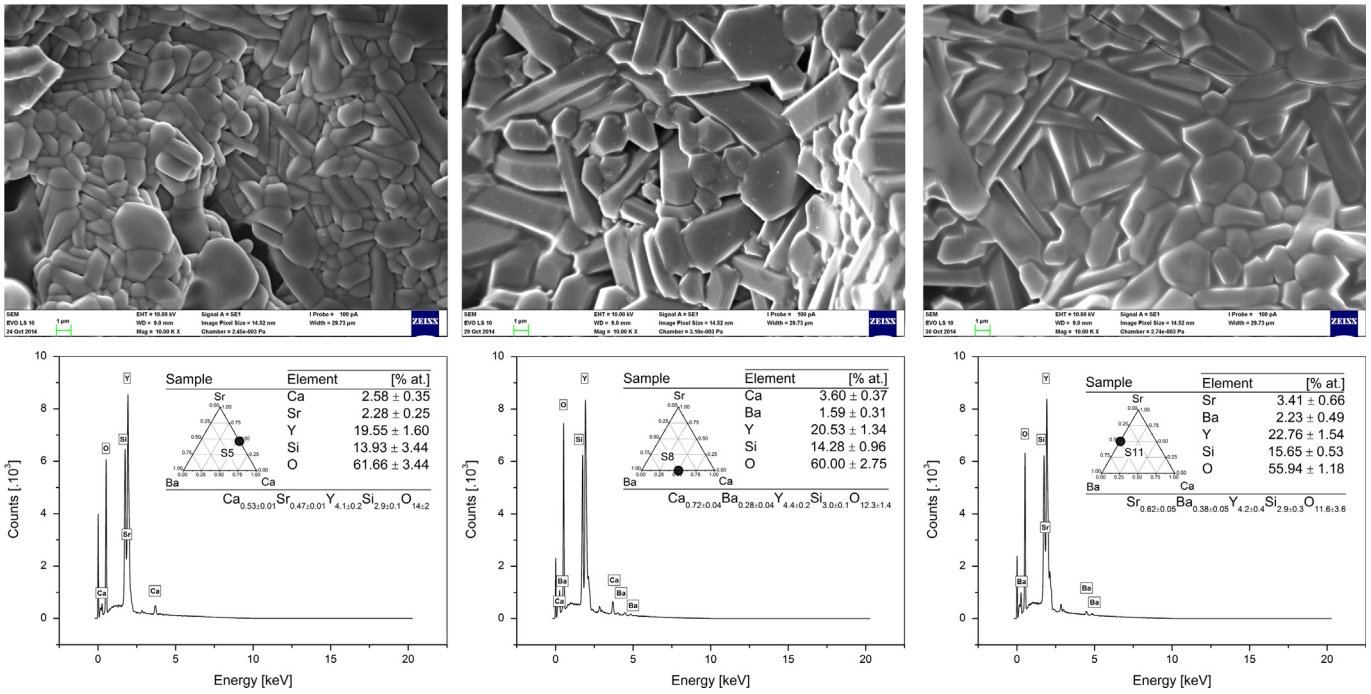

Fig. 8. Scanning electron microscopy and WDX analysis of samples S5 (Ca–Sr series), S8 (Ca–Ba series) and S11 (Sr–Ba series).

Table 2
Variation of parameter δ for pure and binary samples of $AEE_{\delta}Y_{10-\delta}[SiO_4]_6O_{3-0.5\delta}$.

System	Sample	δ	System	Sample	δ
Pure phases	S1	2.02 ± 0.07	$(AEE)_{\delta}Y_{10-\delta}[SiO_4]_3O_{3-0.5\delta}$, AEE=Ca and Ba	S7	1.98 ± 0.12
	S2	1.90 ± 0.04	(binary series II.)	S8	1.99 ± 0.08
	S3	–		S9	2.04 ± 0.34
$(AEE)_{\delta}Y_{10-\delta}[SiO_4]_3O_{3-0.5\delta}$, AEE=Ca and Sr (binary series I., Fig. 2(a))	S4	2.05 ± 0.09	$(AEE)_{\delta}Y_{10-\delta}[SiO_4]_3O_{3-0.5\delta}$, AEE=Sr and Ba (binary series III.)	S10	1.84 ± 0.04
	S5	2.06 ± 0.07		S11	1.95 ± 0.07
	S6	1.90 ± 0.06		S12	2.02 ± 0.05

parameter for the prediction of stability of AEE–yttrium orthosilicate oxybritholites.

Since the composition of prepared samples does not show any significant difference from the system stoichiometry ($\delta \rightarrow 2$), all these samples lie on the same plane (Fig. 12(b)). Based on the existence of $Ca_4Y_6[SiO_4]_6O_2$ apatite-type phase [88,89] ($\delta = 4$), at least one other plane with own field of solid solutions can be expected beyond this plane.

Standard formation energies (ΔH_f°, S° and ΔG_f°, a) and molar heat capacities (b) at 25 °C and 1 bar predicted over investigated field of solid solutions are introduced by Table 4. The effect of AEE can be expressed by the order: Ca, Sr and Ba, where increasing content of left element increases the thermodynamic stability of $AEE_{\delta}Y_{10-\delta}[SiO_4]_6O_{3-0.5\delta}$ (ss) and decreases its molar heat capacity. The values of $c_{p,m}^{\circ}$ calculated from the contribution of cation and anion (Latimer [82,83]) are in good agreement with these results.

The change of lattice parameters (a, c, a:c and V) with the composition of prepared solid solutions (Fig. 13(a)) was determined from XRD pattern (b). Since the trivalent REE cations show strong preference for the M(2) position in synthetic apatites and oxyapatites [84,90], the structure of prepared $AEE_2Y_8[SiO_4]_6O_2$ samples is more similar to $NaY_9(SiO_4)_6O_2$ [90] than to $Ca_2Ce_8(SiO_4)_6O_2$ oxyapatite [86]. The volume of elemental unit cell increases with increasing content of cation with higher atomic number, i.e. in the order: Ca, Sr and Ba. The highest value ($V = 531.90$ Å^3) is then located on the cross solid solution area borderline with Sr–Ba side (binary series III.) of ternary diagram.

The results of infrared spectroscopy (Fig. 14) show the same pattern for all prepared samples. The spectrum consists of five bands with the most characteristic vibration mode at the wavenumber 940.1 ± 3.1 cm^{-1}. Other four bands are located at 562.6 ± 0.8, 511.8 ± 1.1, 477.6 ± 0.3 and 435.7 ± 0.8 cm^{-1}. These bands show the average intensity ratio of 1:0.77 (± 0.02):0.74 (± 0.01):0.61 (± 0.09):0.59 (± 0.03). Based on our previous investigation [34], on literature [91,92] and with the consideration of composition of prepared oxybritholites, where only the features of Si tetrahedra and Y polyhedrons can be expected over investigated range of IR region, the most expressive (first) band is recognized as triply-degenerated $\nu_3(F_2)$ asymmetrical stretching mode of Si–O bond in SiO_4 tetrahedra. The band shows composed structure (Fig. 14(b)) which results from overlapping of modes of different symmetry (**1–3**). The weak bands at

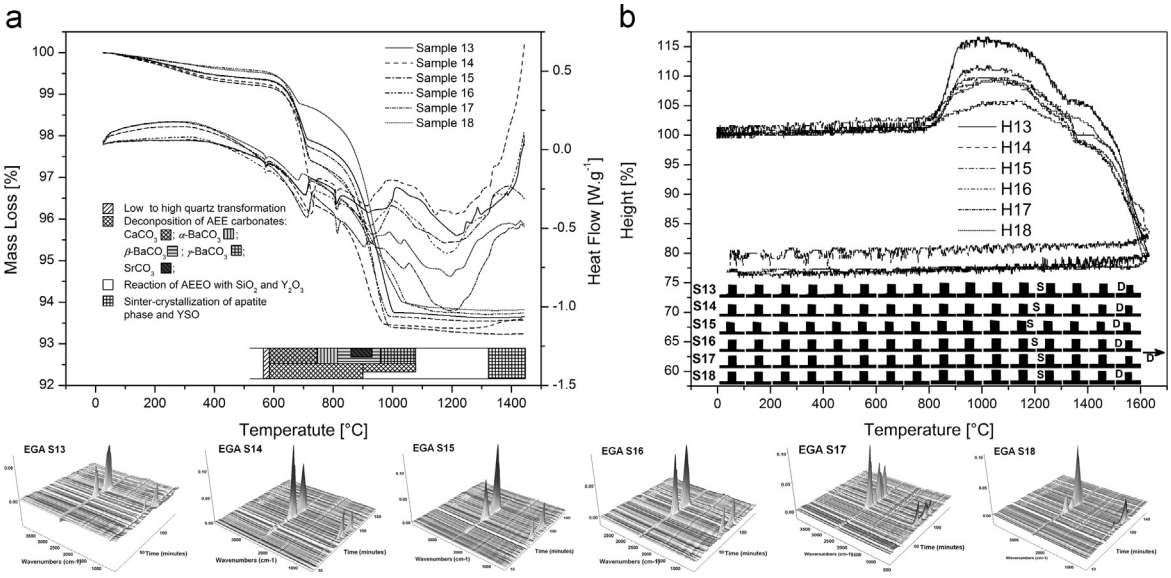

Fig. 9. Simultaneous TG–DTA and EGA (a) and heating microscopy (b) of ternary system specimens.

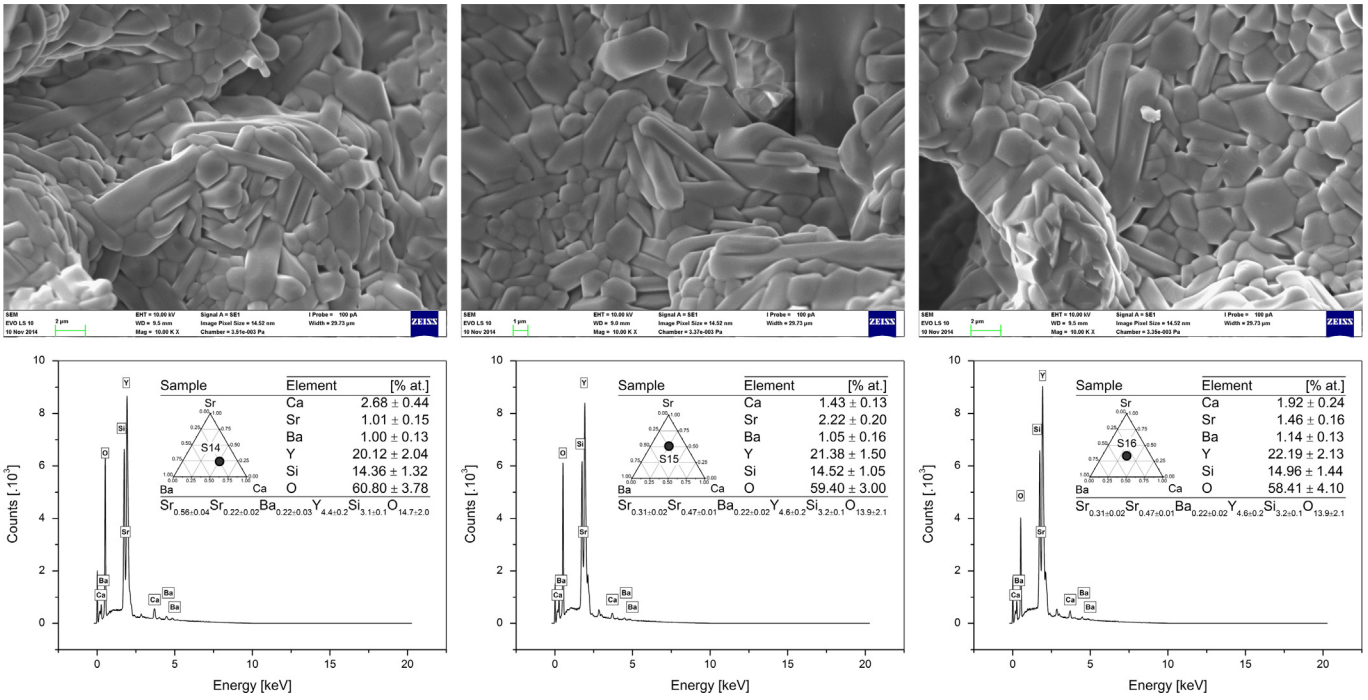

Fig. 10. Samples within or close to the border of miscibility region.

1091 and 797 cm^{-1} are assigned to $\nu_3(F_2)$ asymmetrical stretching in glassy-like phase (***G***, please referee to the discussion of Fig. 5) and to symmetrical stretching vibration ($\nu_1(A_1)$) of Si–O bond, respectively. Other four bands in infrared spectrum were assigned as shown in Fig. 14(a).

While the position of $\nu_3(F_2)$ band is affected by the composition of sample, other peaks are not changed significantly. The highest wavenumber of this mode can be observed for sample S1 (949.3 cm^{-1}) and the lowest one for sample S11 (929.0 cm^{-1}). This behavior could be explained by geometrical distortion in apatite-type lattice caused by increasing repulsive interaction between Si^{4+} and AEE^{2+} ion(s). Removing of degeneracy of $\nu_3(F_2)$ mode leads to increased intensity of complexity of this band. This explanation is in agreement with the effect of increasing ionic radius from Ca to Ba as well as with the effect of r^{2+}_{AEE}/r^{4+}_{Si} ratio on the stability of solid solution (Fig. 12(c)). On the other hand the behavior is also affected by the distribution of yttrium and then also AEE^{2+} ions between M(1) and M(2) positions as was disused above.

The theoretical density of oxybritholites samples (Fig. 2) was calculated ($\rho_t = \boldsymbol{M} \cdot \boldsymbol{Z}/\boldsymbol{V} \cdot \boldsymbol{N}_A$, where $\boldsymbol{Z}=2$ and $\boldsymbol{N}_A = 6.022 \cdot 10^{23}$ mol^{-1}) from the data of molar mass (Fig. 12(a)) and volume of

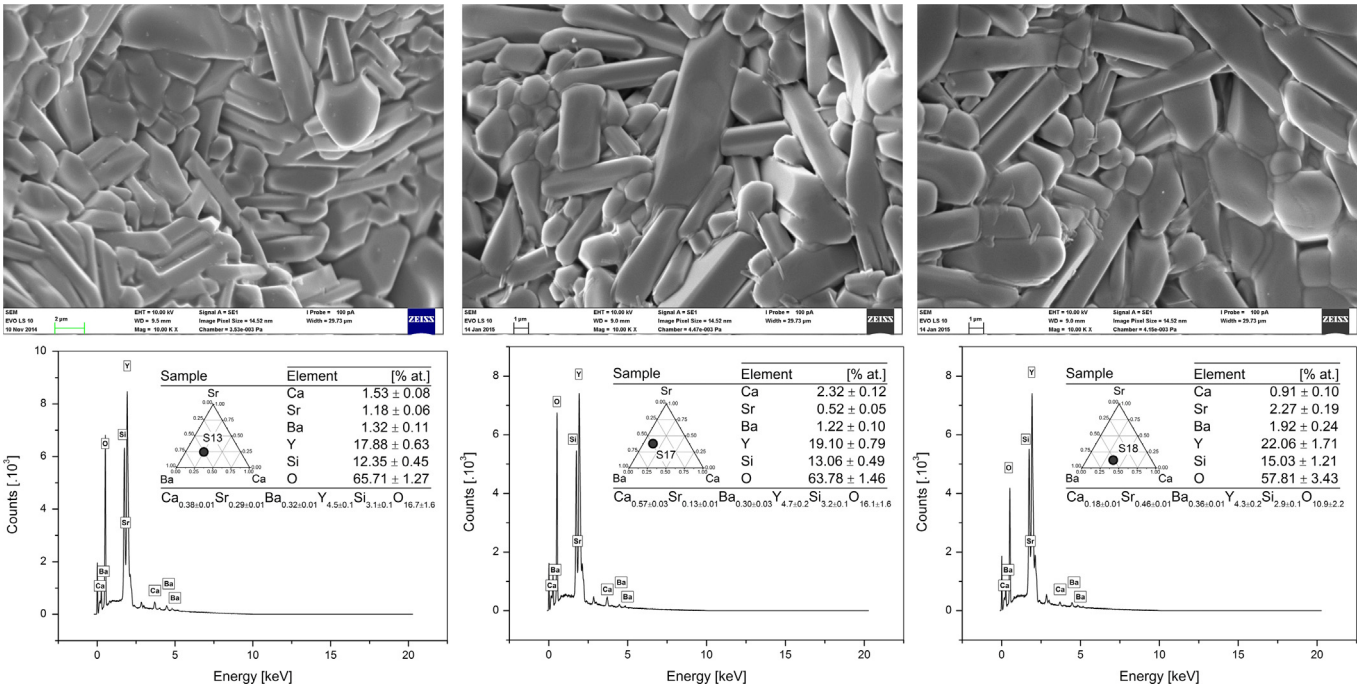

Fig. 11. Samples with the composition out of the border of miscibility region.

Table 3
Variation of parameter δ in the $AEE_{\delta}Y_{10-\delta}[SiO_4]_6O_{3-0.5\delta}$ ternary system.

Sample	S13	S14	S15	S16	S17	S17
δ	1.95 ± 0.05	1.94 ± 0.08	1.92 ± 0.07	1.81 ± 0.05	1.87 ± 0.05	2.02 ± 0.06

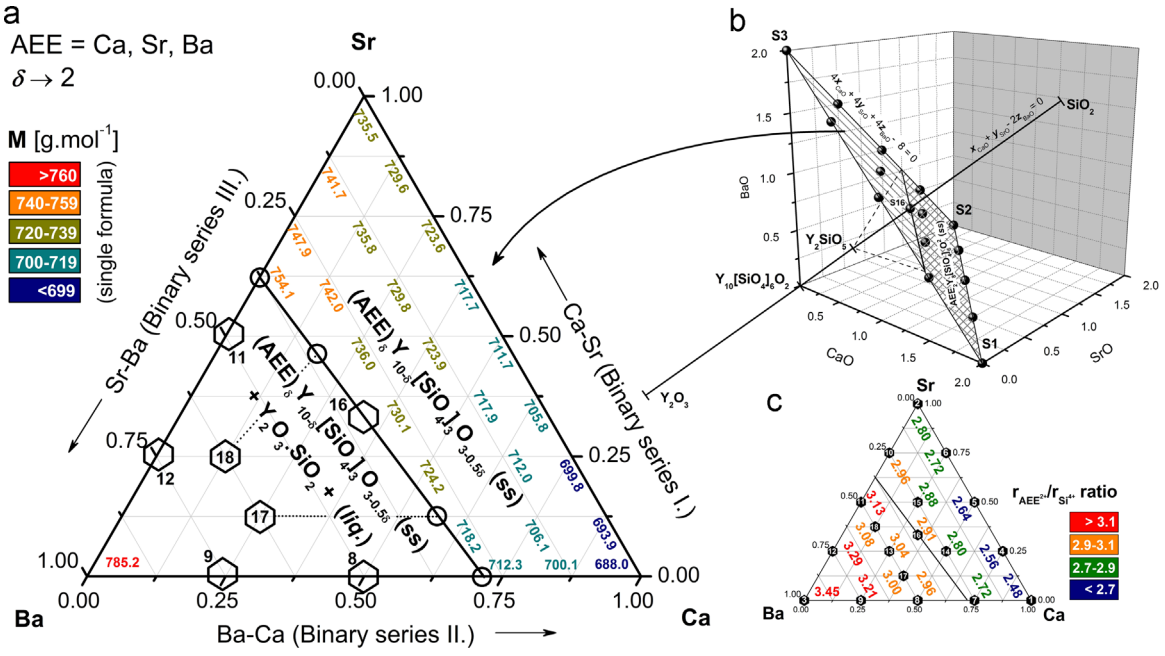

Fig. 12. Field of solid solutions (a) in the ternary apatite-type system of $AEE_{\delta}Y_{10-\delta}[SiO_4]_6O_{3-0.5\delta}$ (AEE=Ca, Sr and Ba and $\delta \rightarrow 2$). Details (b) and (c) show the sketch (not in scale) of location of these compounds in more general phase equilibrium system, and the values of r^{2+}_{AEE}/r^{4+}_{Si} ionic radius ratio, respectively.

Table 4
Estimation of standard formation potentials at 298 K and 1 bar and molar heat capacity.

Parameter[a]		S4	S5	S6	S7	S10	S14	S15	S16
ΔH_f°	[kJ mol^{-1}]	−14.664	−14.658	−14.652	−14.652	−14.634	−14.646	−14.640	14.638
S°	[J (mol K)$^{-1}$]	698.6	705.9	713.3	702.5	724.4	709.9	717.3	716.1
ΔG_f°	[kJ mol^{-1}]	−14.872	−14.868	−14.864	−14.681	−14.850	−14.857	−14.853	−14.851
$c_{p,m}^\circ$	[J (mol K)$^{-1}$]	732.1	733.5	734.9	732.6	736.2	734.0	734.5	735.1
$c_{p,m}^{\circ}$ [b]		728.4	728.8	729.2	728.8	729.7	729.3	729.7	729.6

[a]Values estimated for end-member compositions are listed in Table 1.
[b]Calculated by Latimer method.

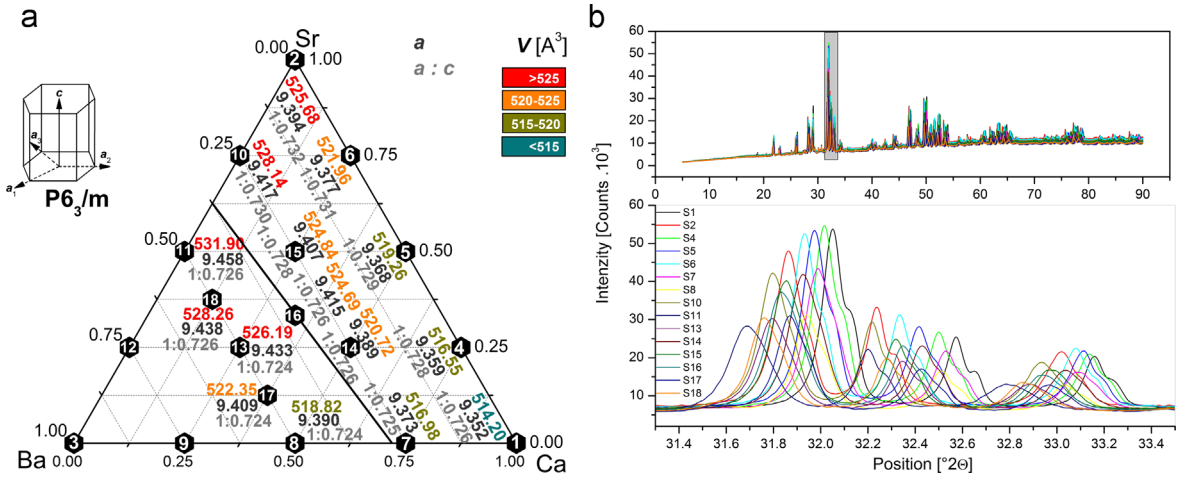

Fig. 13. The dependence of unit cell parameters on the composition of solid solutions (a) and XRD analysis of oxybritholite specimens (b).

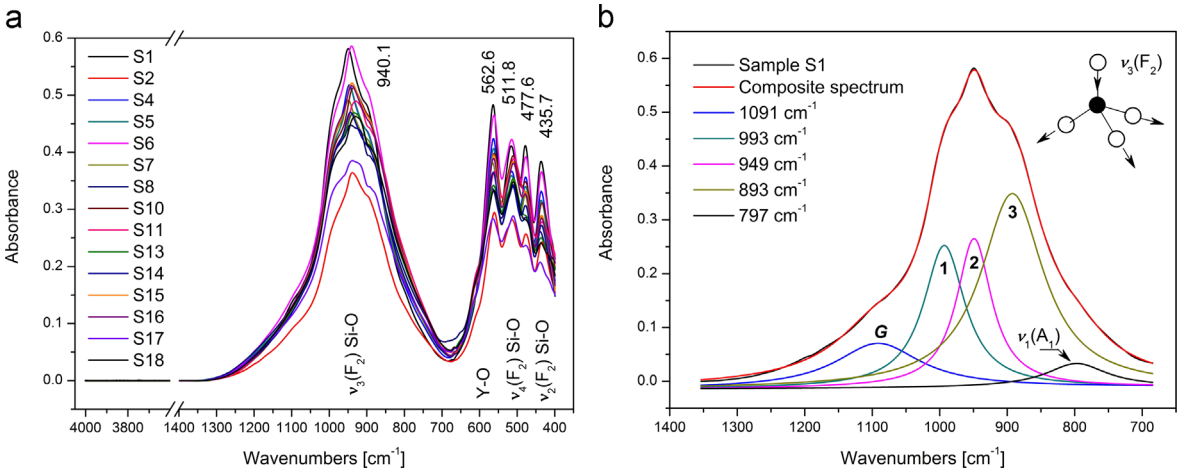

Fig. 14. IR analysis of oxybritholite specimens (a) and fitting of $\nu_3(F_2)$ band by Lorentzian function (b).

elemental unit cell (Fig. 13(a)). It is introduced in Fig. 15 (a) together with other determined properties, i.e. thermal conductivity (λ) and average linear expansion coefficient α_L(25–1500 °C) of prepared apatite specimens. Measured values of λ and α_L as well as high thermal stability (please consult with the results of heating microscopy) predestine the utilization of these oxybritholites (primarily $Ca_2Y_8(SiO_4)_6O_2$) as ceramics with low expansion coefficient, i.e. the materials with good thermal shock resistance. Depending on their composition and mechanical treatment the samples show green, orange or dark blue luminescence (Fig. 15(b)).

4. Conclusion

Alkaline earth element-yttrium-silicate oxybritholites with the structure of apatite form the field of solid solutions of $(Ca_xSr_yBa_z)Y_{10-\delta}[SiO_4]_6O_{3-0.5\delta}$ (where $x+y+z=\delta$) where the limiting value of parameter z was determined to be 28%

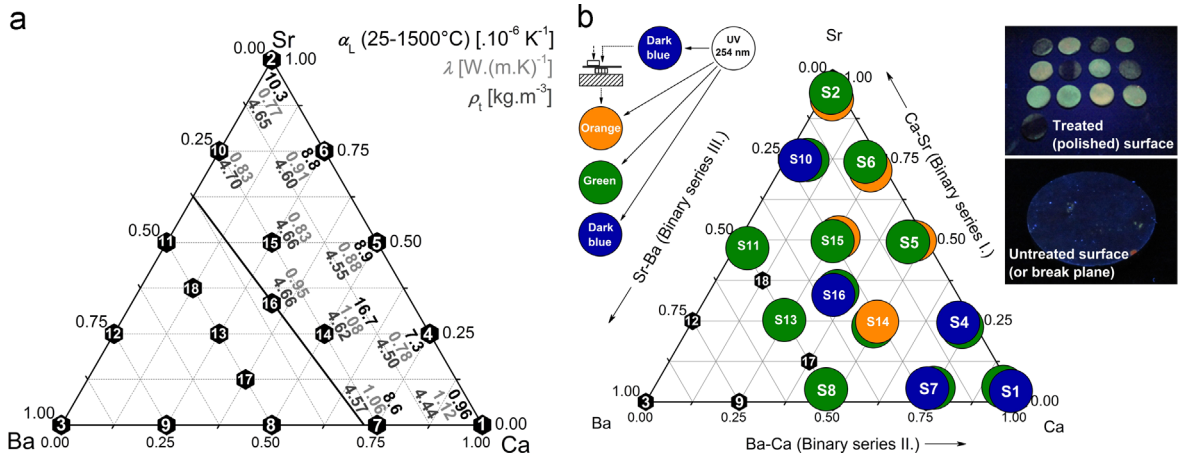

Fig. 15. Influence of composition on the value of λ and α_L (a). Color of luminescence observed under UV light (254 nm) radiation (b).

and 38% for $Ca_2Y_8[SiO_4]_6O_2$ and $Sr_2Y_8[SiO_4]_6O_2$ end-member, respectively. Since all attempts for the synthesis of $Ba_2Y_8[SiO_4]_6O_2$ phase via the ceramic route were not successful, it may be prepared only in a solid solution where r^{2+}_{AEE}/r^{4+}_{Si} ionic radius ratio is ≥ 2.96. The stability of solid solution then decreases with increasing value of ionic radius ratio as the consequence of geometrical distortion caused by increasing repulsive interactions between Si^{4+} and AEE^{2+} ion(s).

The selectivity of Ca-bearing minerals for REE and low preference of Y for M(2) site [84] decrease the limiting content of barium in binary Ba–Ca and ternary solid solutions compared to the system of Sr–Ba. The miscibility between $Ca_2Y_8[SiO_4]_6O_2$ and $Sr_2Y_8[SiO_4]_6O_2$ constituents is not limited. The composition of all prepared specimens of alkaline earth element-yttrium-silicate oxybritholites is close to stoichiometric one ($\delta \approx 2$).

Within the field of solid solutions composition, $AEE_2Y_8[SiO_4]_6O_2$ crystallizes in the form of hexagonal prisms terminated by basal pinacoid. The variation of lattice parameters shows that the volume of elemental cell increases with increasing content of alkaline earth element of higher atomic number. Good thermal stability of sintered specimens, together with their other determined properties including the average linear expansion coefficient and the thermal conductivity enable the utilization in preparation of refractory ceramics with low expansion coefficient.

Acknowledgments

The paper has been supported by project Materials Research Centre at FCH BUT- Sustainability and Development, REG LO1211, with financial support from National Programme for Sustainability I (Ministry of Education, Youth and Sports).

References

[1] M. Jacobson, R.J. Charlson, H. Rodhe, G.H. Orians, Earth System Science: From Biogeochemical Cycles to Global Changes, Academic Press, 2000.

[2] S.J. Van Kauwenbergh, World Phosphate Rock Reserves and Resources, International Center for Soil Fertility and Agricultural Development, Alabama, 2010.

[3] C. Drouet, A comprehensive guide to experimental and predicted thermodynamic properties of phosphate apatite minerals in view of applicative purposes, J. Chem. Thermodyn. 81 (2015) 143–159.

[4] J. Gómez-Morales, M. Iafisco, J.M. Delgado-López, S. Sarda, C. Drouet, Progress on the preparation of nanocrystalline apatites and surface characterization: overview of fundamental and applied aspects, Prog. Cryst. Growth Charact. Mater. 59 (1) (2013) 1–46.

[5] M. Tourbin, A. Al-Kattan, C. Drouet, Study on the stability of suspensions based on biomimetic apatites aimed at biomedical applications, Powder Technol. 255 (2014) 17–22.

[6] A. Al-Kattan, S. Girod-Fullana, C. Charvillat, H. Ternet-Fontebasso, P. Dufour, J. Dexpert-Ghys, V. Santran, J. Bordère, B. Pipy, J. Bernad, C. Drouet, Biomimetic nanocrystalline apatites: emerging perspectives in cancer diagnosis and treatment, Int. J. Pharm. 423 (1) (2012) 26–36.

[7] P. He, S.-N. Takeshima, S. Tada, T. Akaike, Y. Ito, Y. Aida, pH-sensitive carbonate apatite nanoparticles as DNA vaccine carriers enhance humoral and cellular immunity, Vaccine 32 (47) (2014) 6199–6205.

[8] S. Sumathi, B. Gopal, A new insight into biomedical applications of an apatite like oxyphosphate – $BiCa_4(PO_4)_3O$, Ceram. Int. 41 (3, Part B) (2015) 4852–4860.

[9] W.L. Suchanek, P. Shuk, K. Byrappa, R.E. Riman, K.S. TenHuisen, V. F. Janas, Mechanochemical–hydrothermal synthesis of carbonated apatite powders at room temperature, Biomaterials 23 (3) (2002) 699–710.

[10] H.K. Varma, S. Suresh Babu, Synthesis of calcium phosphate bioceramics by citrate gel pyrolysis method, Ceram. Int. 31 (1) (2005) 109–114.

[11] L. Joosu, A. Lepland, K. Kirsimäe, A.E. Romashkin, N.M.W. Roberts, A. P. Martin, A.E. Črne, The REE-composition and petrography of apatite in 2 Ga Zaonega Formation, Russia: the environmental setting for phosphogenesis, Chem. Geol. 395 (2015) 88–107.

[12] M. He, H. Shi, X. Zhao, Y. Yu, B. Qu, Immobilization of Pb and Cd in contaminated soil using nano-crystallite hydroxyapatite, Procedia Environ. Sci. 18 (2013) 657–665.

[13] R. Yu, N. Xue, T. Wang, Z. Zhao, J. Wang, Z. Hei, M. Li, H. Mi Noh, J. Hyun Jeong, Photoluminescence characteristics of high thermal stable fluorosilicate apatite $Ba_2Y_3(SiO_4)_3F:Sm^{3+}$ orange–red emitting phosphor, Ceram. Int. 41 (4) (2015) 6030–6036.

[14] M.A. Pogosova, D.I. Provotorov, A.A. Eliseev, M. Jansen, P.E. Kazin, Synthesis and characterization of the Bi-for-Ca substituted copper-based apatite pigments, Dyes Pigm. 113 (2015) 96–101.

[15] M. Gruselle, Apatites: a new family of catalysts in organic synthesis, J. Organomet. Chem. 793 (2015) 93–101.

[16] P. Chen, R.K. Li, Two high terbium content apatites: $Tb_5Si_2BO_{13}$ and $Tb_{4.66}Si_3O_{13}$, J. Alloy. Compd. 622 (2015) 859–864.

[17] A.G. Werner, Kurze Klassifikation und Beschreibung der verschiedenen Gebirgsarten, Walther, Dresden, 1787.

[18] C.-X. Li, Y.-H. Duan, W.-C. Hu, Electronic structure, elastic anisotropy, thermal conductivity and optical properties of calcium apatite $Ca_5(PO_4)_3X$ (X=F, Cl or Br), J. Alloy. Compd. 619 (2015) 66–77.

[19] M. Pasero, A.R. Kampf, C. Ferraris, I.V. Pekov, J. Rakovan, T.J. White, Nomenclature of the apatite supergroup minerals, Eur. J. Mineral. 22 (2) (2010) 163–179.

[20] E. Kreidler, F. Hummel, The crystal chemistry of apatite: structure field of fluor- and chlorapatite, Am. Mineral. 55 (1970) 170–184.

[21] L. Boyer, J. Carpena, J.L. Lacout, Synthesis of phosphate–silicate apatites at atmospheric pressure, Solid State Ion. 95 (1–2) (1997) 121–129.

[22] R. El Ouenzerfi, M.-T. Cohen-Adad, C. Goutaudier, G. Panczer, Uranium-doped britholites $Ca_xLay(SiO_4)_{6-u}(PO_4)_uO_f$:U synthesis, characterization and preliminary study of uranium diffusion, Solid State Ion. 176 (2005) 225–231.

[23] E. Valsami-Jones, I.W. Association, Phosphorus in Environmental Technologies: Principles and Applications, IWA Publishing, 2004.

[24] A. Alper, Refractory materials: a series of monographs, in: A.M. Alper (Ed.), Phase Diagrams, Academic Press, 1978, p. ii.

[25] J. Ito, Siliate apatites and oxyapatites, Am. Miner. 53 (1968) 890–907.

[26] L. León-Reina, J.M. Porras-Vázquez, E.R. Losilla, M.A.G. Aranda, Phase transition and mixed oxide-proton conductivity in germanium oxyapatites, J. Solid State Chem. 180 (4) (2007) 1250–1258.

[27] S. Habelitz, L. Pascual, A. Durán, Nitrogen-containing apatite, J. Eur. Ceram. Soc. 19 (15) (1999) 2685–2694.

[28] S.M. Hosseini, T. Shvareva, A. Navrotsky, Energetics of lanthanum silicate apatite: influence of interstitial oxygen and cation vacancy concentrations in $La_{9.33+x}(SiO_4)_6O_{2+3x/2}$ and $La_{10-x}Sr_x(SiO_4)_6O_{3-0.5x}$, Solid State Ion. 233 (2013) 62–66.

[29] P.J. Panteix, E. Béchade, I. Julien, P. Abélard, D. Bernache-Assollant, Influence of anionic vacancies on the ionic conductivity of silicated rare earth apatites, Mater. Res. Bull. 43 (5) (2008) 1223–1231.

[30] K. Sudarsanan, R.A. Young, A.J.C. Wilson, The structures of some cadmium 'apatites' $Cd_5(MO_4)_{3X}$. I. Determination of the structures of $Cd_5(VO_4)_3I$, $Cd_5(PO_4)_3Br$, $Cd_3(AsO_4)_3Br$ and $Cd_5(VO_4)_3Br$, Acta Crystallogr. Sect. B: Struct. Sci. 33 (10) (1977) 3136–3142.

[31] Q. Shi, L. Lu, H. Jin, H. Zhang, Y. Zeng, Electrical properties and thermal expansion of cobalt doped apatite-type lanthanum silicates based electrolytes for IT-SOFC, Mater. Res. Bull. 47 (3) (2012) 719–723.

[32] E.G. Nordström, K.H.B.M.E.- Karlsson, Chemical characterization of a potassium hydroxyapatite prepared by soaking in potassium chloride and carbonate solutions, Biomed. Mater. Eng. 2 (4) (1992) 185–189.

[33] S. Lahrich, M.A. Elmhammedi, B. Manoun, Y. Tamraoui, F. Mirinioui, M. Azrour, P. Lazor, Elaboration, Rietveld refinements and vibrational spectroscopic study of $Na_{1-x}K_xCaPb_3(PO_4)_3$ lacunar apatites ($0 \le x \le 1$), Spectrochim. Acta Part A 145 (2015) 493–499.

[34] P. Ptáček, E. Bartoníčková, J. Švec, T. Opravil, F. Šoukal, J. Wasserbauer, J. Másilko, Preparation, kinetics of sinter-crystallization and properties of hexagonal strontium–yttrate–silicate apatite phase: $SrY_4[SiO_4]_3O$, Ceram. Int. 41 (1, Part B) (2015) 1779–1795.

[35] H. Kiyono, Y. Matsuda, T. Shimada, M. Ando, I. Oikawa, H. Maekawa, S. Nakayama, S. Ohki, M. Tansho, T. Shimizu, P. Florian, D. Massiot, Oxygen-17 nuclear magnetic resonance measurements on apatite-type lanthanum silicate ($La_{9.33}(SiO_4)_6O_2$), Solid State Ion. 228 (2012) 64–69.

[36] S. Lambert, A. Vincent, E. Bruneton, S. Beaudet-Savignat, F. Guillet, B. Minot, F. Bouree, Structural investigation of $La_{9.33}Si_6O_{26-\delta}$ and $La_9AESi_6O_{26+\delta}$-doped apatites-type lanthanum silicate (AE=Ba, Sr and Ca) by neutron powder diffraction, J. Solid State Chem. 179 (8) (2006) 2602–2608.

[37] M. Gaft, R. Reisfeld, G. Panczer, G. Boulon, S. Shoval, B. Champagnon, Accommodation of rare-earths and manganese by apatite, Opt. Mater. 8 (1–2) (1997) 149–156.

[38] L. Calderín, M.J. Stott, A. Rubio, Electronic and crystallographic structure of apatites, Phys. Rev. B: Condens. Matter 67 (13) (2003) 134106.

[39] A.P. Tyutyunnik, G.V. Bazuev, Synthesis, crystal structure and magnetic properties of $Sr_5(CrO_4)_3(Cu_{0.586}O)$ with apatite-like structure, J. Alloy. Compd. 522 (2012) 141–143.

[40] T. Baikie, Z. Ahmad, M. Srinivasan, A. Maignan, S.S. Pramana, T. J. White, The crystallographic and magnetic characteristics of Sr_2CrO_4 (K_2NiF_4-type) and $Sr_{10}(CrO_4)_6F_2$ (apatite-type), J. Solid State Chem. 180 (5) (2007) 1538–1546.

[41] J.E.H. Sansom, P.R. Slater, Oxide ion conductivity in the mixed Si/Ge apatite-type phases $La_{9.33}Si_{6-x}Ge_xO_{26}$, Solid State Ion. 167 (1–2) (2004) 23–27.

[42] A. Breithaupt, Bestimmung neuer mineral-specien, hedyphan, J. Chem. Phys. 60 (1830) 308–316.

[43] L.S. Borodin, M.E. Kezarova, Belovite – a new mineral from an alkaline pegmatite, Dokl. Akad. Nauk SSSR 96 (1954) 613–616.

[44] I.V. Pekov, N.V. Chukanov, O.V. Beletskaya, A.P. Khomyakov, Y. P. Menshikov, Belovite-(Ce): new data, refined formula and relationship to other minerals of the apatite group, Zap. RMO 124 (1995) 98–110.

[45] C. Winther, Britholite, a new mineral, Monogr. Greenl. 24 (1901) 190–196.

[46] E.H. Nickel, J.D. Grice, The IMA commission on new minerals and mineral names: procedures and guidelines on mineral nomenclature, 1998, Mineral. Petrol. 64 (1–4) (1998) 237–263.

[47] S. Hata, Abukumalite, a new yttrium mineral, Sci. Pap. Inst. Phys. Chem. Res. 34 (1938) 1018–1023.

[48] D. McConnell, The substitution of SiO_4^- and SO_4^- groups for PO_4^- groups in the apatite structure; ellestadite, the end-member, Am. Mineral. 22 (1937) 977–986.

[49] B.V. Chesnokov, L.F. Bazhenova, A.F. Bushmakin, Fluorellestadite $Ca_{10}[(SO_4),(SiO_4)]_6F_2$—a new mineral, Zap. RMO 116 (6) (1987) 743–746.

[50] R.C. Rouse, P.J. Dunn, A contribution to the crystal chemistry of ellestadite and silicate sulfate apatites, Am. Mineral. 67 (1982) 90–96.

[51] C.A. Gerhards, V. Erster Ahnung, Von einigen noch nicht genau bestimmten und ganz neu entdecken Mineralien, in: C.A. Gerhards (Ed.), Grundriss des Mineralsystems, Christian Friedrich Himburg, Berlin, 1786, pp. 281–287.

[52] C.F. Rammelsberg, Apatit, in: Handbuch der Mineralchemie, Wilhelm Engelmann, Leipzig, 1860, pp. 351–355.

[53] A. Damour, Notice sur l'hydro-apatite: espèce minérale, in: Annales des Mines, vol. 10, 1856.

[54] E.A.J. Burke, Tidying up mineral names: an IMA-CNMNC scheme for suffixes, hyphens and diacritical marks, Miner. Rec. 39 (2008) 131–135.

[55] M. Mehmel, Uber die Struktur des Apatits, Z. Krist. 75 (1930) 323–331.

[56] S. Náray-Szabó, The structure of apatite $(CaF)Ca_4(PO_4)_3$, Z. Krist. 75 (1930) 387–398.

[57] V. Uvarov, S. Shenawi-Khalil, I. Popov, New bismuth calcium oxysilicate with apatite structure: synthesis and structural characterization, J. Solid State Chem. 183 (7) (2010) 1484–1489.

[58] J.M. Hughes, M. Cameron, K.D. Crowley, Structural variations in natural F, OH, and Cl apatites, Am. Mineral. 74 (1989) 870–876.

[59] S.C. Lim, T. Baikie, S.S. Pramana, R. Smith, T.J. White, Apatite metaprism twist angle (φ) as a tool for crystallochemical diagnosis, J. Solid State Chem. 184 (11) (2011) 2978–2986.

[60] A.P. Shpak, V.L. Karbovskii, N.A. Kurgan, Peculiarities of the electronic structure of calcium and strontium apatites, J. Electron Spectrosc. Relat. Phenom. 156–158 (2007) 457–462.

[61] A.R. Chakhmouradian, L. Medici, Clinohydroxylapatite: a new apatite-group mineral from northwestern Ontario (Canada), and new data on the extent of Na–S substitution in natural apatites, Eur. J. Mineral. 18 (1) (2006) 105–112.

[62] P.C. Piilonen, R. Rowe, T.S. Ercit, A.J. Locock, New mineral names, Am. Mineral. 91 (2006) 1452–1457.

[63] D.C. Noe, J.M. Hughes, A.N. Mariano, J.W. Drexler, A. Kato, The crystal structure of monoclinic britholite-(Ce) and britholite-(Y), Z. Krist. 206 (1993) 233–246.

[64] N. Kalsbeek, S. Larsen, J.G. Ronsbo, Crystal structures of rare earth elements rich apatite analogues, Z. Krist. 191 (1990) 249–263.

[65] J. Zhao, X. Dong, M. Bian, J. Zhao, Y. Zhang, Y. Sun, J. Chen, X. Wang, Solution combustion method for synthesis of nanostructured hydroxyapatite, fluorapatite and chlorapatite, Appl. Surf. Sci. 314 (2014) 1026–1033.

[66] N. Kamel, H. Aït-Amar, A. Zahri, The use of a soaking procedure combined with the sintering process to reach a high cerium content in a cerium-bearing Y-britholite, Prog. Nucl. Energy 49 (4) (2007) 351–364.

[67] H. Njema, M. Debbichi, K. Boughzala, M. Said, K. Bouzouita, Structural, electronic and thermodynamic properties of britholites $Ca_{10-x}La_x(PO_4)_{6-x}(SiO_4)_xF_2$ $(0 \le x \le 6)$: experiment and theory, Mater. Res. Bull. 51 (2014) 210–216.

[68] H. Shanshan, T. Wanjun, Single-phased white-light-emitting $Sr_3NaLa(PO_4)_3F$: Eu^{2+},Mn^{2+} phosphor via energy transfer, J. Lumin. 145 (2014) 100–104.

[69] A. Onda, S. Ogo, K. Kajiyoshi, K. Yanagisawa, Hydrothermal synthesis of vanadate/phosphate hydroxyapatite solid solutions, Mater. Lett. 62 (8–9) (2008) 1406–1409.

[70] O. Frank-Kamenetskaya, A. Kol'tsov, M. Kuz'mina, M. Zorina, L. Poritskaya, Ion substitutions and non-stoichiometry of carbonated apatite-(CaOH) synthesised by precipitation and hydrothermal methods, J. Mol. Struct. 992 (1–3) (2011) 9–18.

[71] H. Zhang, Q. Zhu, Structure control in hydroxyapatite synthesis by hydrothermal reaction and organic modulators, China Part 3 (6) (2005) 317–320.

[72] Y.-P. Guo, T.-S. Lin, Y. Zhou, D.-C. Jia, Y.-J. Guo, Fabrication of monodisperse mesoporous hydroxycarbonate apatite microspheres by emulsion method, Microporous Mesoporous Mater. 127 (3) (2010) 245–249.

[73] M.G. Zuev, A.M. Karpov, AS. Shkvarin, Synthesis and spectral characteristics of $Sr_2Y_8(SiO_4)_6O_2$: Eu polycrystals, J. Solid State Chem. 184 (1) (2011) 52–58.

[74] R.J. Ackermann, C.A. Sorrell, Thermal expansion and the high-low transformation in quartz. I. High-temperature X-ray studies, J. Appl. Crystallogr. 7 (5) (1974) 461–467.

[75] P. Ptáček, Strontium Aluminate – Cement Fundamentals, Manufacturing, Hydration, Setting Behaviour and Applications, InTech Europe, Rijeka, Croatia, 2014.

[76] P. Ptáček, E. Bartoníčková, J. Švec, T. Opravil, F. Šoukal, F. Frajkorová, The kinetics and mechanism of thermal decomposition of $SrCO_3$ polymorphs, Ceram. Int. 41 (1, Part A) (2015) 115–126.

[77] S.M. Antao, I. Hassan, $BaCO_3$: high-temperature crystal structures and the Pmcn→R3m phase transition at 811 °C, Phys. Chem. Miner. 34 (8) (2007) 573–580.

[78] S.M. Antao, I. Hassan, The orthorhombic structure of caco3, srco3, pbco3 and baco3: linear structural trends, Can. Mineral. 47 (5) (2009) 1245–1255.

[79] I. Arvanitidis, D. Siche, S. Seetharaman, A study of the thermal decomposition of $BaCO_3$, Metall. Mater. Trans. B 27 (3) (1996) 409–416.

[80] Y. Parganiha, J. Kaur, V. Dubey, D. Chandrakar, Synthesis, characterization, thermoluminescence and optical studies of Eu^{3+} doped Y_2SiO_5 phosphor, Superlattices Microstruct. 77 (2015) 152–161.

[81] C. Cannas, M. Mainas, A. Musinu, G. Piccaluga, S. Enzo, M. Bazzoni, A. Speghini, M. Bettinelli, Structural investigations and luminescence properties of nanocrystalline europium-doped yttrium silicates prepared by a sol–gel technique, Opt. Mater. 29 (6) (2007) 585–592.

[82] W.M. Latimer, Methods of estimating the entropies of solid compounds, J. Am. Chem. Soc. 73 (4) (1951) 1480–1482.

[83] G.K. Moiseev, J. Sestak, Some calculations methods for estimation of thermodynamical and thermochemical properties of inorganic compounds, Prog. Cryst. Growth Charact. Mater. 30 (1) (1995) 23–81.

[84] M.E. Fleet, Y. Pan, Site preference of rare earth elements in fluorapatite, Am. Minerol. 80 (1995) 329–335.

[85] H. Takeda, M. Ohgaki, T. Kizuki, K. Hashimoto, Y. Toda, S. Udagawa, K. Yamashita, Formation mechanism and synthesis of apatite-type structure $Ba_{2+x}La_{8-x}(SiO_4)_6O_{2-\delta}$, J. Am. Ceram. Soc. 83 (11) (2000) 2884–2886.

[86] J.M.S. Skakle, C.L. Dickson, F.P. Glasser, The crystal structures of $CeSiO_4$ and $Ca_2Ce_8(SiO_4)_6O_2$, Powder Diffr. 15 (04) (2000) 234–238.

[87] N.A. Toporov, N.F. Fedorov, Composition diagram of the Ca_2SiO_4–$Y_4(SiO_4)_3$ system, Zh. Neorg. Khim. 10 (1965) 666–668.

[88] G. Li, Y. Zhang, D. Geng, M. Shang, C. Peng, Z. Cheng, J. Lin, Single-composition trichromatic white-emitting $Ca4Y_6(SiO_4)_6O$: Ce^{3+}/Mn^{2+}/Tb^{3+} phosphor: luminescence and energy transfer, ACS Appl. Mater. Interfaces 4 (1) (2012) 296–305.

[89] W.L. Wanmaker, J.W. Vrugt, J.G. Verlijsdonk, Synthesis of new compounds with apatite structure, Philips Res. Rep. 26 (1971) 373–381.

[90] R.P. Gunawardane, R.A. Howie, F.P. Glasser, Structure of the oxyapatite $NaY_9(SiO_4)_6O_2$, Acta Crystallogr. Sect. B: Struct. Sci. 38 (5) (1982) 1564–1566.

[91] B. Saikia, G. Parthasarathy, N.C. Sarmah, Fourier transform infrared spectroscopic estimation of crystallinity in SiO_2 based rocks, Bull. Mater. Sci. 31 (5) (2008) 775–779.

[92] W.R. Taylor, Application of infrared spectroscopy to studies of silicate glass structure: examples from the melilite glasses and the systems Na_2O–SiO_2 and Na_2O–Al_2O_3–SiO_2, Proc. Indian Acad. Sci. (Earth Planet. Sci.) 99 (1) (1990) 99–117.